Crossover from fractal to compact flow from simulations of two-phase flow with finite viscosity ratio in two-dimensional porous media

M. Ferer,* W. N. Sams,† R. A. Geisbrecht,‡ and Duane H. Smith†,§
Morgantown Energy Technology Center, Morgantown, West Virginia 26507-0880
(Received 25 September 1992)

The effect of the viscosity ratio ($M \equiv \mu_D/\mu_I$) in changing the nature of viscous fingering was studied using a simple, physical model of miscible, dispersionless, two-phase, linear flow in model two-dimensional porous media. For all viscosity ratios, the initial flows had an unstable, fractal character which crossed over to stable, compact flow on a time (or length) scale which increased with the viscosity ratio. An empirical scaling of the data enables an asymptotic characterization of both this time scale $\tau \approx M^{\phi_t}$, where $\phi_t = 0.17 \pm 0.03$, as well as the front velocity $v \approx M^{\epsilon\phi_t}$ where $\epsilon\phi_t = 0.07 \pm 0.02$. A comparison with identical simulations of radial flow indicates that the same characteristic length scale applies in both linear and radial geometries $l \approx M^{\phi_l}$ where $\phi_l = 0.24 \pm 0.06$, while the time scales differ because of the different relations between time and size in the two geometries.

PACS number(s): 82.20.Wt, 47.55.Mh, 47.10.+g, 68.10.−m

I. INTRODUCTION

Many recent papers have addressed various aspects of fractal growth phenomena [1–10], including the fractal nature of the viscous fingering that arises when an injected fluid with low viscosity (μ_I) is used to displace a "defending" fluid with larger viscosity (μ_D). A central concern is the determination of what factors affect the nature of this growth, what factors change the value of the fractal dimension, and what factors change the growth from fractal to compact. As with any real problem, there are a number of possibly relevant parameters for changing the nature of two-phase flow in porous media. Earlier work [4,11] showed that the amount of fingering increased with the viscosity ratio to fractal growth at infinite viscosity ratio, whereas the growth was obviously compact for small viscosity ratios. Indeed, it has been shown that the limit of infinite viscosity ratio ($M \equiv \mu_D/\mu_I \to \infty$) is correctly described by diffusion-limited aggregation (DLA), a process which is known to form fractal objects with nonuniform densities [6,12].

Early work showed that increasing the amount of disorder in the porous medium changes the nature of the growth from dendritic to random [2]. Later, for immiscible fluids it was shown that increasing the wetting by the invading fluid increases the width of the viscous fingers, with a transition to compact growth occurring at a "critical" contact angle [5]. Modified DLA simulations have shown that a finite capillary number induces a crossover from invasion percolationlike flow to DLA-like flow [10]. Lack of isotropy in the porous medium yields visibly anisotropic patterns and effects a small change in the fractal dimension from $D_f \approx 1.63$ for two-dimensional, isotropic systems to $D_f \approx 1.7$ for simulations on a square lattice [9,12]. It is the transition for miscible fluids from DLA-like fractal growth to compact growth with decreasing viscosity ratio ($M \equiv \mu_D/\mu_I$) that we have attempted to characterize. In order to delineate clearly the effect of the viscosity ratio, we have assumed zero surface tension (consistent with miscible fluids) and negligible dispersion (mixing) of these fluids to maintain a sharp interface.

These questions are especially relevant to oil recovery and reservoir simulation because all traditional field simulations of oil reservoirs are based upon a Darcy's-law treatment using saturation-dependent relative permeabilities [13]. As used in engineering applications, Darcy's law involves a mean-field-like averaging of the microscopic equations suppressing fluctuations which are known to modify asymptotic behavior in other applications [14]. Indeed, the results of asymptotic fractal flow are contrary to the basic engineering assumption of saturation-dependent fractional flows and relative permeabilities [15]. Thus, it is crucial to determine whether or not the real, finite-viscosity-ratio flow is fractal or compact. Experiments and simulations have shown that the viscosity ratio does effect a crossover from fractal flow at large viscosity ratios to compact flow at small viscosity ratios [4,11]. However, these studies did not attempt to characterize or even locate the crossover. In an earlier paper ([16], hereafter referred to as I), we performed deterministic simulations of radial flow which located and crudely characterized the crossover. In this longer paper, we will study linear flow which provides improved statistics, allowing us to characterize more convincingly the crossover for both flow geometries, which will allow characterization of the fractional flows [15].

It is useful to review some of the characteristics of fractals. The classic signature of a fractal object is a non-Euclidean relationship between mass and size. For a "circular" fractal object in d dimensions, the mass is proportional to R^{D_f}, where $D_f < d$ (e.g., for two-dimensional DLA, $D_f \approx 1.70 \pm 0.06$) [12]. For linear flow in the x direction, the mass of the injected fluid, which is proportional to the time [17], varies as the $D_f - 1$ power of the linear size as long as the average linear size x is much less than the width of the system. Therefore, mass is approxi-

mately equal to x^{D_f-1}; for a DLA-like fractal,

$$\langle x \rangle \approx t^{1.4} , \tag{1}$$

where time t has replaced the mass and we have used the value of the fractal dimension for on-lattice DLA [6]. In the formation of fractals, the patterns initially have many small fingers, some of which grow faster than others. The longer fingers grow more rapidly than the short fingers, so that as the object grows, it coarsens (i.e., it has fewer and fewer growing fingers). Therefore, at an advanced stage of growth the pattern has many fingers on many different size scales, giving a nonuniform density, provided that the system is wide enough. For a system of finite width w, the pattern will eventually evolve to a stage where there is only one growing finger, whose length is comparable to the system width; at this stage the growth will appear linear or stable (pseudostable) because all growth occurs in the one dominant finger. A number of excellent reviews discuss a wide variety of these fractal growth phenomena including material deposition, dielectric breakdown, and two-phase flow, the topic of this paper [6,18,19].

In modeling miscible two-phase flow in porous media, we have sought the most standard and most physically rigorous model possible; a detailed discussion is presented in Sec. II. Briefly, we used a standard square-lattice model of homogeneous two-dimensional porous media [2,4,20] in which the pore bodies, at the sites of a square lattice, all have unit volume but the cross-sectional area of each pore throat is randomly chosen from a uniform distribution; this distribution is known to give random, fractal flow for infinite viscosity ratio [2]. For miscible flow, there is zero interfacial tension so that the flow velocity through any pore throat is proportional to pressure drop across the throat as defined by Poiseuille's law. Furthermore, we assume zero dispersion, assuring a well-defined interface in our model flows. Determining the conductances (or transmissibilities) from Poiseuille's law, we then use a slight modification of the standard Gauss-Seidel iteration of the discrete Laplace equation until the residual is less than 10^{-5}. Knowing the pressure drops across the throats and the conductances enable us to determine the flow rate for each throat. We then use straightforward deterministic flow rules to advance the interface through a short time Δt. The upper bound on the residuals and the flow rules, to be described shortly, were found to satisfy total fluid conservation to within 0.5%, even after 1400 time steps. This procedure has the advantage of not suppressing fractal flow [4]; indeed, earlier variants of this model were used to study fractal flow [2,7]. As discussed in Sec. III, the large viscosity ratio limit of this model does produce the expected DLA-like fractal flows.

In Sec. IV we address the question, "Is viscous fingering fractal for finite viscosity ratios?" Using the model discussed above and detailed in Sec. II, we study the motion of the interface through the time dependence of the first moment of the injected fluid, i.e., $\langle x(t) \rangle_M$, for the finite viscosity ratios $M=3$ to 300. For these viscosity ratios, and probably for all finite viscosity ratios, the simulations produce initial fractal flows obeying Eq. (1) which become compact (or linear),

$$\langle x \rangle_M = v(M)t , \tag{2}$$

on a characteristic time scale which increases with the viscosity ratio. It is shown that the fractal to compact "crossover" can be convincingly characterized by a heuristic fractal scaling of our data for $\langle x(t) \rangle_M$, which enables us to characterize the viscosity-ratio dependence of the characteristic time $\tau(M)$ and the "front" velocity $v(M)$. It seems likely that our assumption of negligible dispersion will be a worst-possible-case scenario for fractal-to-compact crossover in miscible floods, because dispersion would smooth the interface, thereby favoring compact flow and accelerating any fractal-to-compact crossover.

In Sec. V, we compare these results for the linear flow geometry with our earlier results for the radial flow geometry [15]. We find that the characteristic size scale associated with the fractal-to-compact crossover is asymptotically the same for both geometries, while the crossover times obey different power laws because of the different relations between size and fractal mass (or time) in the two geometries. These simulations for finite viscosity ratio show initial fractal advance of the interface followed by an overshoot and "overdense" relaxation to stable flow on a scale which could be characterized by an asymptotic, power-law dependence upon the viscosity ratio.

II. DESCRIPTION OF THE MODEL

In modeling two-dimensional porous media, we have used a variant of a standard square-lattice representation [2,4,8,20,21]. This $N_x \times N_y$ square-lattice model has pore bodies, of unit volume, at the lattice sites $\mathbf{r}=(2m,2n)$ for all integers $m=1 \rightarrow N_x$ and $n=1 \rightarrow N_y$. These pore bodies are connected by cylindrical throats of unit length, at the vertical and horizontal bond locations $\mathbf{r}=(2m+1,2n)$ and $(2m,2n+1)$, respectively. The randomly chosen cross-sectional areas of these throats are uniformly distributed in the interval 0 to 1. This broad distribution assures that the growth will be chaotic rather than dendritic [2]. Furthermore, the finite volume of the throats allows for realistically smooth variations in the conductance of a throat as it becomes invaded, which is not the case in models where a zero-volume throat is either occupied or unoccupied [2,21].

To ascertain the effects of a finite viscosity ratio, we assume Poiseuille flow through a throat, neglecting the surface tension effects of capillary pressure and wetting. Poiseuille's law relates the pressure drop (ΔP) across a throat and the volume flow rate (q) through that throat, e.g., for the throat at $\mathbf{r}=(2m+1,2n)$,

$$\begin{aligned} &\Delta P_{2m+1,2n} = q_{2m+1,2n} / T_{2m+1,2n} , \\ &P_{2m,2n} - P_{2m+2,2n} \\ &\quad = \left\{ \frac{\mu_I x_{2m+1,2n} + \mu_D (1 - x_{2m+1,2n})}{C r^4_{2m+1,2n}} \right\} q_{2m+1,2n} , \end{aligned} \tag{3}$$

where T is the transmissibility (or conductance) of the throat, x is the length (fraction of the unit length) of throat invaded and r is the radius of this throat, and C is a constant. Imposing volume conservation for our incompressible fluids requires that the net volume flow into any pore body must be zero, e.g., for the pore body at $(2m,2n)$,

$$\sum_{\delta} q_{(2m,2n)+\delta}=0 , \tag{4}$$

where the sum is over all nearest-neighbor displacement vectors, specifically, $\delta=(1,0)$, $(-1,0)$, $(0,1)$, and $(0,-1)$. Using Poiseuille's Law, Eq. (3) in Eq. (4), one finds a discretized Laplace's equation, which can be written in the familiar form

$$P_{(2m,2n)}=\sum_{\delta} T_{(2m,2n)+\delta}P_{(2m,2n)+2\delta}\Big/\sum_{\delta} T_{(2m,2n)+\delta} , \tag{5}$$

where we have chosen boundary conditions with a high pressure at the inlet pore bodies at $x=0$ ($P_{0,2n}=100$); zero pressure at the outlet edge ($P_{2N_x+2,2n}=0$), and zero-flow conditions on the sides ($T_{2m,1}=T_{2m,2N_y+1}=0$). To find iterative solutions for the pressure field, we have used a slight variant of the standard over-relaxed Gauss-Seidel scheme such that the normalized residuals $\mathcal{R}$,

$$\mathcal{R}=\sum_{m,n}\left\{\sum_{\delta} q_{(2m,2n)+\delta}\Big/\sum_{\delta} T_{(2m,2n)+\delta}\right\}^2 ,$$

fall below a confidence limit which we have normally chosen to be 10^{-5} or 10^{-6}. These confidence limits plus the flow rules described below satisfy overall fluid conservation to within a fraction of a percent (i.e., we find differences which are typically less than 0.5% when we compare the total volume of invading fluid in the porous medium up to breakthrough with the volume of displaced fluid).

Having (i) defined the porous medium, (ii) determined the conductances, (iii) solved iteratively for the initial pressure field, and (iv) found the initial volume flows in the pore throats, we can now advance the interface through some short time interval Δt. We have chosen a Δt such that the interface advances one-half pore-body volume (i.e., one-half unit) in that interface throat with the maximum volume flow rate, i.e., $q_{\max}\Delta t=\frac{1}{2}$. The flow rules allow the interface to advance through throats such that the flow is from a fully invaded pore body towards a pore body which is not yet fully invaded. As shown in Fig. 1(a), this advance can occur within the pore throat, into the pore body, or through the pore body into the adjacent outflow throats. These flow rules also allow the interface to retreat locally through throats where the flow is from a pore body which is not fully invaded towards a pore body which is fully invaded (or was fully invaded and is not yet completely defender-filled). As shown in Fig. 1(b), this retreat can occur within the pore throat, into a fully invaded pore body, or even through a pore body into the outflow throats.

We then cycle this process by (i) finding the transmissibilities for the new interface location, (ii) solving for the new pressure field, (iii) determining the new volume flow rates, and (iv) advancing the interface through $\Delta t=1/(2q_{\max})$ until breakthrough when the interface reaches the edge of the porous medium. Our largest models consist of $90\times300=27\,000$ pore bodies; for these largest systems, to reach breakthrough, we find that we must cycle this process from as few as 700 times to as many as 1400 times, depending on the viscosity ratio and on the individual porous medium. The longest of these runs use 21 h of computer CPU time on a floating-point-system (FPS) vector array processor. To assure that our time scale $\Delta t=1/(2q_{\max})$ was not too coarse, we also performed some trial runs for $\Delta t=1/(4q_{\max})$. The results for this finer time scale were indistinguishable from those for the more efficient, coarser time scale in that results for the moments were statistically indistinguishable and the patterns appear similar.

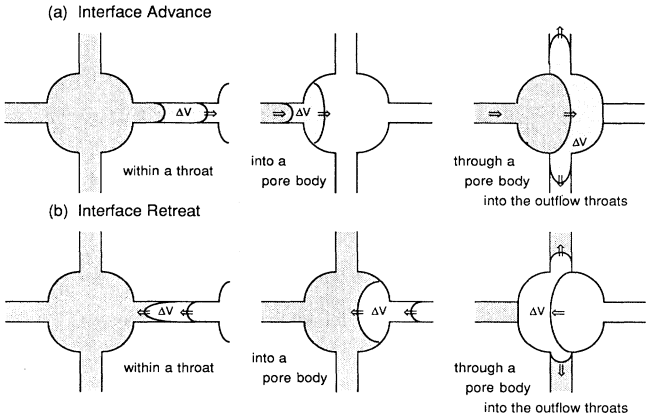

FIG. 1. Flow rules: (a) The flow can cause the interface to advance through a volume $\Delta V=u\Delta t$ within a pore throat, from the pore throat into the connected pore body, and from the pore body into the outflow throats. (b) The flow can cause the interface to retreat through a volume $\Delta V=u\Delta t$ within a pore throat, from the pore throat into the connected pore body, and from the pore body into the outflow throats.

III. FRACTAL BEHAVIOR AT INFINITE VISCOSITY RATIO

Next, we will show that our modeling produces fractal flow for a large viscosity ratio, enabling us to check the predictions in Eqs. (1). Using a viscosity ratio of 10 000, we ran our modeling program up to breakthrough for 17 different realizations of our model porous medium, all of which were $N_y=300$ pore bodies wide. Each of these realizations was generated by starting with a different seed for the random-number generator on our FPS machine. Of these 17 different realizations, 11 were $N_x=60$ pore bodies long and 6 were $N_x=90$ pore bodies long. Figure 2 shows a typical, near-breakthrough pattern for one of the 90×300 porous media; this pattern appears to be fractal, having fingers of many different sizes and looking very much like the patterns from DLA

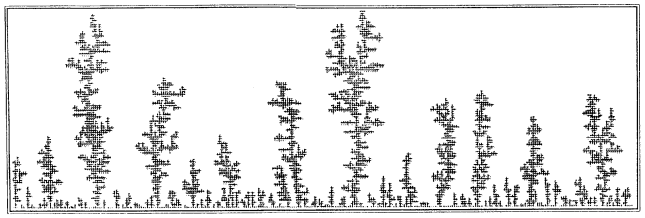

FIG. 2. Near-breakthrough flow pattern showing the pore bodies and throats occupied by injected fluid for a 90×300 porous medium resulting from our simulations with a fluid viscosity ratio $M=10\,000$.

simulations [6]. We purposely chose to model the flow on short-wide systems to avoid the pseudostable flow produced in long-narrow systems by the dominance of one single finger. Furthermore, the 17 short-wide media provide statistics comparable to 75 square porous media (i.e., 55 60×60 media and 20 90×90 media) because both have the same number of pore bodies.

During each of these runs, we have determined the time (mass of injected fluid) and first moment $\langle x\rangle$ at each time step. In order to verify that this large a viscosity ratio ($M=10\,000$) yields fractal flows in our model, we have studied the dependence of $\langle x\rangle$ upon t. Figure 3 shows the log-log plot of $\langle x\rangle/t^{1.4}$ vs t. Our specific definition of t is proportional to the total volume of injected fluid $V_{\rm tot}$ (also proportional to the total mass) through the relation

$$t=1.3+(V_{\rm tot}/N_y)\ . \tag{6}$$

For this linear problem, where low-viscosity fluid is injected into all the N_y inlet pore bodies along the width, the factor of N_y in Eq. (6) accounts for the width dependence of the injection rate, allowing us to compare systems of different widths used in some of the later simulations. As discussed in the Appendix, the additive factor of 1.3 can be understood as arising from the difference between our inherently discrete model and the more physical continuous systems. In any case, the effect of the factor of 1.3 is insignificant at later times, and serves only to minimize early time curvature in Fig. 3. If the flow is a DLA-like fractal, $\langle x\rangle/t^{1.4}$ will be constant for all t. The points track the results from runs on individual, porous-media realizations. Finite-size effects seem negligible in the near-breakthrough data, since results for the smaller systems near breakthrough (near $t\approx17$, the 60×300 models reach breakthrough) are statistically indistinguishable from results for the larger systems (90×300) in their far-from-breakthrough regimes. This lack of finite-size effects has been verified for all viscosity ratios, more convincingly so for some of the other values where we have simulations for a greater range of lengths and breakthrough times. The solid circles show the results of a data-smoothing procedure in which a quadratic least-squares fit of all the data $[y=\ln(\langle x\rangle/t), x=\ln t]$ with $x=\ln t$ in the interval $(\ln t_i-\frac{1}{4},\ln t_i+\frac{1}{4})$ gives the location of the ith solid circle $[(\langle x\rangle/t)_i, t_i]$ and its standard error. We then let $\ln t_i$ scan the full range of the data. The standard errors are no bigger than the solid circles used in Fig. 3. The first moment does, indeed, show fractal scaling $\langle x\rangle\propto t^{1.4}$, which from Eq. (1) is consistent with the DLA value of the fractal dimension $D_f\approx1.7$. To estimate our certainty in the value of 1.4, we plotted $\langle x\rangle/t^{1.45}$ and $\langle x\rangle/t^{1.35}$; on the scale of Fig. 3, these were clearly tilted from the horizontal. Therefore, we estimate

$$1+\epsilon\equiv1/(D_f-1)=1.40\pm0.05\ ,$$

indicating $D_f=1.71\pm0.04$; these results from our model are in good agreement with the on-lattice DLA value of the fractal dimension $D_f=1.70\pm0.06$ [12].

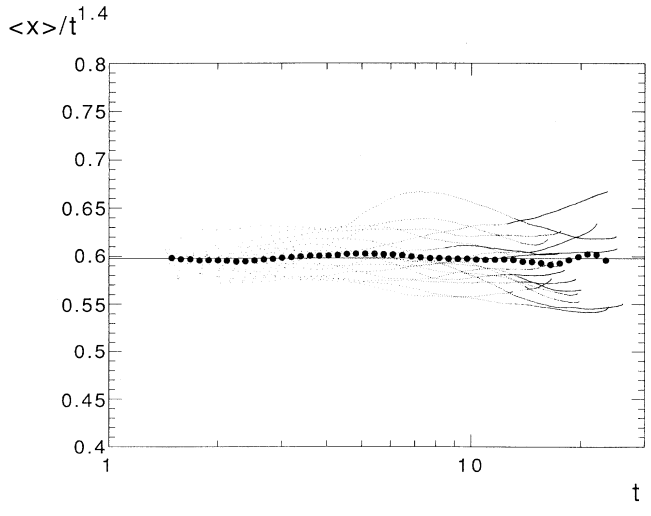

FIG. 3. Fractal behavior of the first moment (i.e., $\langle x\rangle=Ct^{1.4}$) from modeling large viscosity-ratio flows with $M=10\,000$ on 17 different realizations of the porous medium. The dots track the flow for individual realizations, while the solid circles result from the data-smoothing procedure.

IV. IS VISCOUS FINGERING FRACTAL FOR FINITE VISCOSITY RATIOS?

To study the nature of large-scale flows for a finite viscosity ratio, we have modeled flows for smaller viscosity ratios: $M=3$, 10, 30, 100, and 300. For each viscosity ratio, we have used a number of different realizations of our model porous medium to improve statistics. Figure 4 shows the near-breakthrough flow pattern for three different viscosity ratios; this figure demonstrates the previously observed tendency of large-viscosity-ratio flows to appear fractal while small-viscosity-ratio flows are visibly more compact [4]. To quantify the observed crossover from fractal flow to compact flow as a function of viscosity ratio and time, we have determined the first moment of saturation, $\langle x\rangle$, and the time $t=1.3+(V_{\rm tot}/N_y)$, Eq. (5), at each time step in the simulations. Performing these simulations for a number of different realizations of the model porous medium, we smoothed the resulting data, as described in Sec. III, for each viscosity ratio. Figure 5 shows the smoothed data for $\langle x\rangle/t$ versus t for all the

viscosity ratios studied; as before, the standard errors are no larger than the data points. As expected from above, the data for $M=10\,000$ show fractal behavior with $\langle x\rangle/t$ growing as $t^{0.4}$. For the smaller viscosity ratios, the curves initially follow the fractal $t^{0.4}$ dependence; but, beginning with the $M=3$ data, they all break away from the fractal behavior and approach a constant $\langle x\rangle_M/t=v(M)$, characteristic of compact (stable or linear) flow. Furthermore, this breakaway or crossover occurs on a characteristic time scale $\tau(M)$, which increases with the viscosity ratio. In all cases, the flows follow the fractal behavior, overshoot, and then relax back to compact behavior. This intermediate, postovershoot flow has a decreasing $\langle x\rangle/t$, which indicates that, temporarily, the front ($\langle x\rangle$) is advancing more slowly than linearly with time so that the flow is denser than compact. This growth at short distance scales can be verified by observing where the growth occurs during the intermediate, postovershoot regime. Figure 6 shows typical patterns for a viscosity ratio $M=300$ at two times during the flow; the single pixels show occupation and the solid squares show where significant (greater than 2%) growth has occurred in the last few time steps. During the fractal growth stage ($t\approx 10$), the growth occurs primarily at the tips of the longest fingers, consistent with DLA growth. In the denser-than-compact regime ($t\approx 40$), there is significant growth at small distance scales (the interior of the pattern). At a late stage, when the growth is compact, the growth sites would be distributed along the interface. These observations can be made more quantitative by considering the average position of the growth sites:

$$\langle x\rangle_G \equiv \sum_{\mathbf{r}} x\frac{d\rho(\mathbf{r},t)}{dt}\Big/\sum_{\mathbf{r}}\frac{d\rho(\mathbf{r},t)}{dt}\ , \tag{7}$$

where $\rho(\mathbf{r},t)$ is the occupation of the pore body or pore throat at position $\mathbf{r}$ and time t. Since the total injected

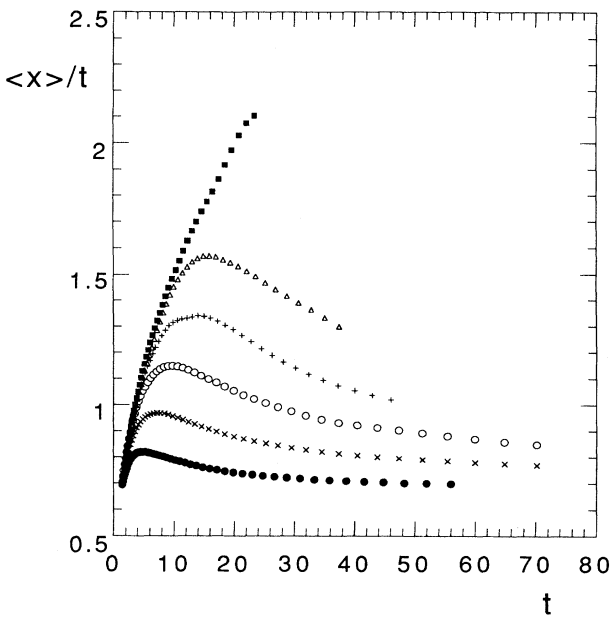

FIG. 5. Smoothed data for $\langle x\rangle/t$ vs t showing the crossover from initial fractal growth ($t^{0.4}$ behavior) to eventual compact growth ($\langle x\rangle/t=v$) with a characteristic time scale increasing with viscosity ratio from $M=3$ (●) to $M=10$ (×), 30 (○), 100 (+), and 300 (△), and eventually to $M=10\,000$ (■), where the crossover has not yet begun.

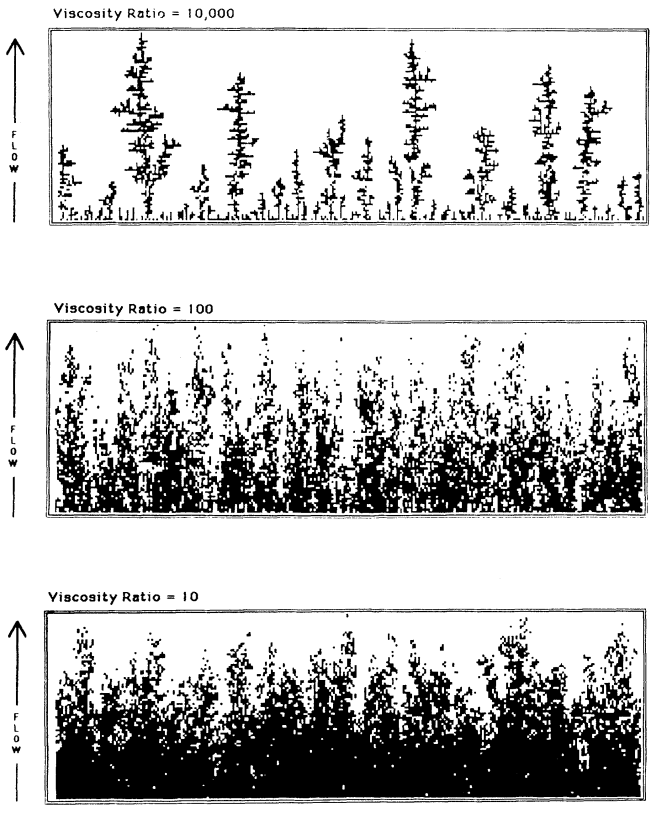

FIG. 4. Near-breakthrough flow patterns show the locations of pore bodies occupied by injected fluid for three different viscosity ratios, $M=10^4$, 10^2, and 10. Note the apparent crossover from fractal to compact flow as the viscosity ratio decreases.

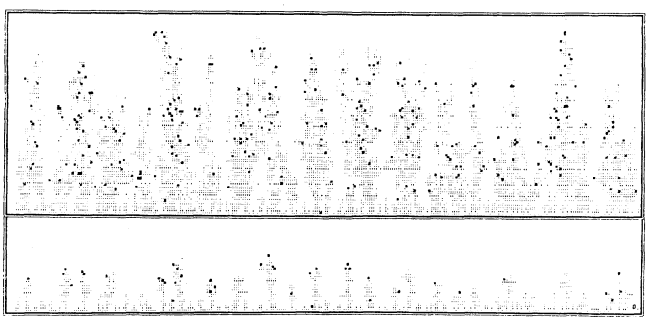

FIG. 6. "Growth zone" for an $M=300$ flow pattern in a typical realization of a 90×300 porous medium. The single pixels show occupation and the solid squares locate recent, significant growth. The bottom figure shows the pattern at $t=10$ during the fractal stage of growth when the growth is occurring primarily at the fingertips; the top figure shows the growth at $t=40$ during the overdense stage when growth is occurring at small distance scales.

mass is our definition of the time, $t=\sum_n \rho(\mathbf{r},t)$, the denominator of Eq. (7) is identically 1. Therefore, $\langle x \rangle_G$ can be determined from the time derivative of $\langle x \rangle$, i.e.,

$$\langle x \rangle_G = t^2 \frac{dt^{-1}\langle x \rangle}{dt} + 2\langle x \rangle \approx \begin{cases} 2.4\langle x \rangle & \text{when } \langle x \rangle / t \approx t^{0.4} \\ 2.0\langle x \rangle & \text{when } \langle x \rangle / t \approx v \ . \end{cases} \quad (8)$$

Thus, when $\langle x \rangle / t$ is constant (compact growth), the growth sites are on the interface, at $2\langle x \rangle$; when $\langle x \rangle / t$ is increasing (fractal growth), the average position of the growth sites is beyond the interface near the tips of the longest fingers; however, when $\langle x \rangle / t$ is decreasing (intermediate, postovershoot growth), the average position of the growth sites is behind the interface, as shown in Fig. 6. Clearly, this denser-than-compact ("overdense") growth cannot be a long-term effect; however, it does represent a real, short-term filling of the voids formed during the fractal stage of growth. In any case, Fig. 5 shows a well-defined crossover from initial fractal growth ($\langle x \rangle / t \approx t^{0.4}$) to eventual compact growth ($\langle x \rangle / t = v$) for all relevant viscosity ratios.

To quantify this process, it is necessary to determine the dependence of front velocity v and characteristic crossover time τ upon the viscosity ratio. We show that the data scale, allowing a convincing characterization of the viscosity-ratio dependence of τ and v. In order to determine a "scaling" variable which will collapse all the data onto a single curve, consider the data for $\langle x \rangle / t^{1.4}$ shown in Fig. 7. All the data start from a value $0.596 = 1/1.678$, characteristic of the fractal dependence, and eventually crossover to the compact behavior with a $t^{-0.4}$ dependence. One can obtain a crude collapse of the data by plotting the data versus a "scaling" variable $t/M^{0.20}$, as shown in Fig. 8, where the characteristic time factor $M^{0.20}$ shifts the large viscosity-ratio data onto the smaller viscosity-ratio data. This estimate for the viscosity-ratio dependence of the relaxation time, i.e., $\tau \approx \tau_0 M^{0.20}$, appears to provide convincing data collapse for large times but not for the intermediate-time regime near $t \approx 10$, where there still remains a small viscosity-ratio-dependent spread of approximately $\Delta t \approx 5$ in the data. Applying a scaling correction which shifts the time origin $\Delta = 8/M^{0.17}$ enabled us to obtain a much more convincing data collapse with the "scaling" variable $u = \{t + \Delta\}/M^{0.17}$, as shown in Fig. 9. It should be noted that the index characterizing the relaxation time changed very little from the value in Fig. 8, i.e., from 0.20 to 0.17. In estimating the reliability of this index, we found that, including the shift, the value 0.20 is now clearly too large and that 0.14 is too small, so that we estimate $\tau \approx \tau_0 M^{\phi_t}$, $\phi_t = 0.17 \pm 0.03$. Not surprisingly, there is less certainty in the exponent associated with the scaling correction Δ in that $M^{0.5}$ is too strong a dependence and $M^{0.01}$ is too weak a dependence. The essential point to retain from this discussion is that the "scaling" variable $u = \{t + (a/M^{\delta})\}/M^{\phi_t}$ provides an excellent empirical collapse of the data for the finite viscosity ratios $M = 3$ to 300 with a value of the relaxation-time index

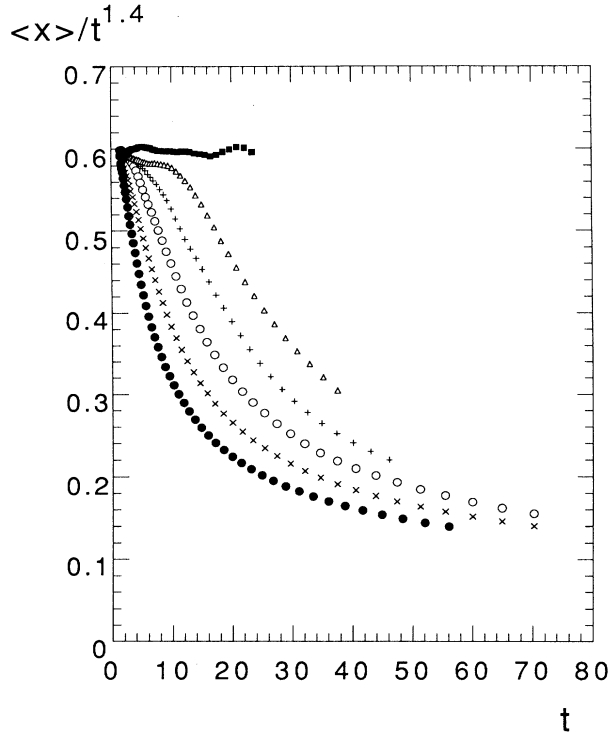

FIG. 7. Plot of $\langle x \rangle / t^{1.4}$ vs t from the smoothed data for all viscosity ratios, showing the crossover from initial fractal behavior (constant) to eventual compact behavior ($t^{-0.4}$ dependence) on a characteristic time scale τ increasing with viscosity ratio [$M = 3$ (●), 10 (×), 30 (○), 100 (+), 300 (△), and 10 000 (■)].

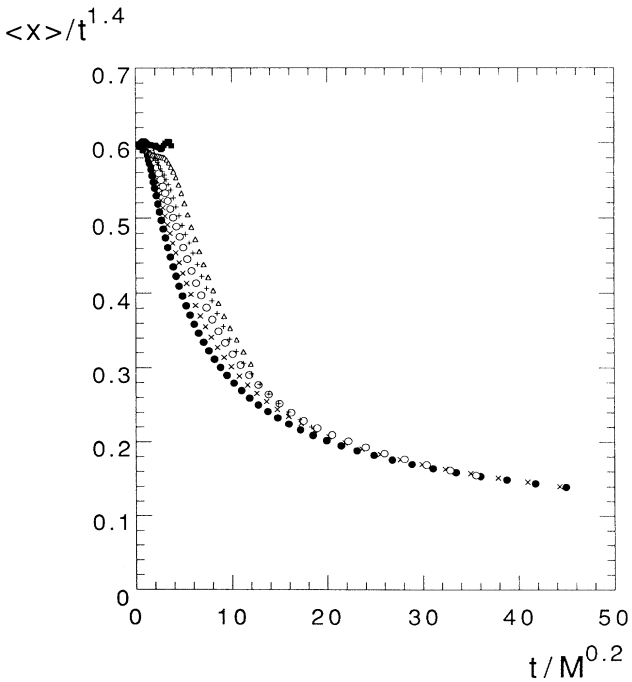

FIG. 8. Plot of $\langle x \rangle / t^{1.4}$ vs $t/M^{0.20}$ showing that a characteristic time which increases with viscosity ratio as $\tau \propto M^{0.20}$ collapses the large-time data, with small deviations approximately $\Delta t \approx 5$ around $t \approx 10$. [$M = 3$ (●), 10 (×), 30 (○), 100 (+), 300 (△), and 10 000 (■)].

$\phi_t = 0.17 \pm 0.03$, so that

$$\langle x \rangle / t^{1.4} = f(u) ,$$
$$u = \{ t + (8/M^{0.17}) \} / M^{0.17} , \tag{9}$$

where $f(u)$ is the function shown in Fig. 9. The value of the shift exponent, $\delta \approx \phi_t$, and the actual form of the shift have no effect on later results and only serve to improve the data collapse. It seems likely that other forms for the shift could provide a data collapse equally convincing, but since the shift must be relatively small ($\Delta < 10$) given the data, having a different shift effecting a significant change in ϕ_t is impossible since that dependence is dominated by long-time behavior.

The dependence of front velocity upon the viscosity ratio can now be determined in a straightforward manner. Since all flows become compact for a finite viscosity ratio in the limit of large times, $\langle x \rangle / t \to v(M)$. Obviously, $\langle x \rangle / t^{1+\epsilon} \to v(M) t^{-\epsilon}$, where $1 + \epsilon \equiv 1/(D_f - 1)$; with Eq. (9) this implies that $f(u) \to v_0 u^{-\epsilon}$, since $u \to t/M^{\phi_t}$. Note that v_0 is a constant independent of the viscosity ratio since, at least empirically from Fig. 9, all the viscosity-ratio dependence is in u, not in the functional form of f. Therefore,

$$\langle x \rangle / t^{1+\epsilon} = f(u) \to v_0 u^{-\epsilon} = v_0 (M^{\phi_t}/t)^{\epsilon} , \tag{10}$$

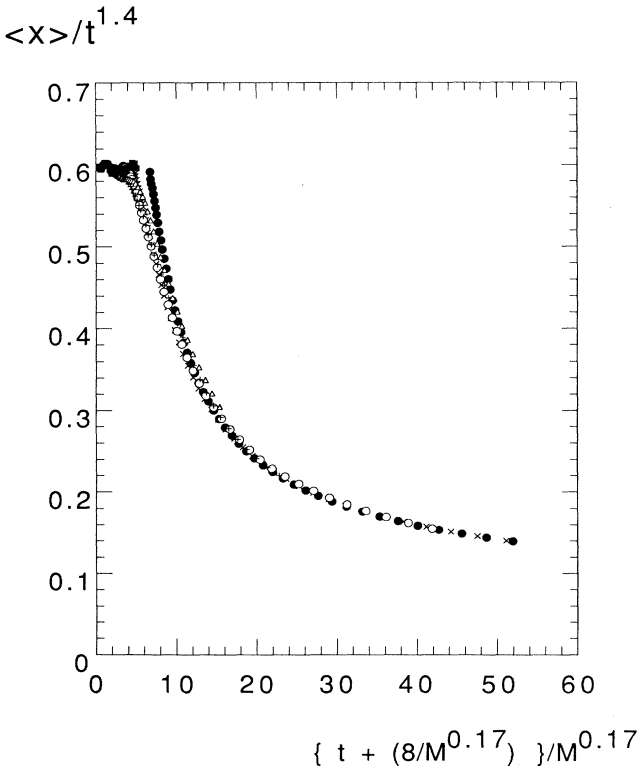

FIG. 9. Scaling plot of $\langle x \rangle / t^{1.4}$ vs $\{ t + 8/M^{0.17} \} / M^{0.17}$ showing that an M-dependent shift $\Delta \approx 8/M^{0.17}$ accommodates the $t \approx 10$ deviations observed in Fig. 7 with only a small change in the power of the characteristic time; now $\tau \propto M^{0.17}$ [$M = 3$ (●), 10 (×), 30 (○), 100 (+), 300 (△), and 10 000 (■)].

so that

$$v(M) = v_0 M^{\epsilon \phi_t} ,$$

where $\epsilon \phi_t = 0.07 \pm 0.02$, given the value $\epsilon = 0.40 \pm 0.05$ and our determination of the relaxation-time exponent ϕ_t.

V. GEOMETRICAL EFFECTS AND RADIAL FLOW

Our linear flow simulations show that the fractal flow crosses over to compact flow on a characteristic time scale which varies asymptotically as $\tau \approx M^{\phi_t}$. Alternatively, one could view the crossover as occurring when the patterns have reached a characteristic size $l \approx M^{\phi_l}$. For linear flow, the characteristic crossover length varies as

$$l \equiv x \approx t^{1/(D_f - 1)} \approx (M^{\phi_t})^{1/(D_f - 1)} ,$$

so that the length and time-based crossover indices are related by $\phi_l = \phi_t / (D_f - 1)$. The values $\phi_t = 0.17 \pm 0.03$ and $D_f = 1.71 \pm 0.06$ predict that the characteristic crossover length $l \approx M^{\phi_l}$ should be characterized by the exponent $\phi_l = 0.24 \pm 0.06$ for linear flow in two dimensions. It remains an open question whether the characteristic crossover time or crossover length is the more fundamental, i.e., which of the two (if either) would characterize the fractal-to-compact crossover in another two-dimensional flow geometry. In I we studied radial flow (central injection) in two dimensions and observed fractal-to-compact crossover, with a characteristic length scale varying approximately as $l \approx M^{\phi_l}$, where $\phi_l \approx \frac{1}{3}$ [16]. In our analysis of the radial flow, the statistics were not nearly as convincing as in the present study for linear flow, and the data did not warrant inclusion of corrections to scaling which slightly decreased the values of ϕ_t in the linear case. Therefore, the uncertainties in our radial flow value of ϕ_l are large enough to admit equality of this value of $\phi_l \approx \frac{1}{3}$ for radial flow to the value $\phi_l = 0.24 \pm 0.06$ for linear flow. For this radial geometry, the relation between characteristic length and time is given by

$$l \equiv R \approx t^{1/D_f} \approx (M^{\phi_t})^{1/D_f} ,$$

so that $\phi_l = \phi_t / D_f$. Therefore, for radial flow, the earlier estimate $\phi_l \approx \frac{1}{3}$ predicts that the time-based crossover exponent should equal $\phi_t \approx 0.566$. This value is nearly quadruple the time-based crossover exponent for linear flow, supporting our conjecture that the length-based crossover exponent $\phi_l = 0.24 \pm 0.06$, not the time-based crossover exponent, is the same for all two-dimensional flow geometries.

Do the radial flow data scale convincingly with a characteristic time which varies asymptotically as $\tau \approx M^{\phi_t} \equiv M^{D_f \phi_l}$, where $\phi_t = \phi_l D_f \approx 0.408$. Figure 10 shows the radial flow data, plotting $R/t^{1/D_f}$ versus t, showing the fractal behavior ($R \approx t^{0.583}$) at small times, and the eventual crossover to compact ($R \approx t^{1/2}$) behavior on a time scale which is increasing with viscosity ratio. Figure 11 shows the scaling of the data, now

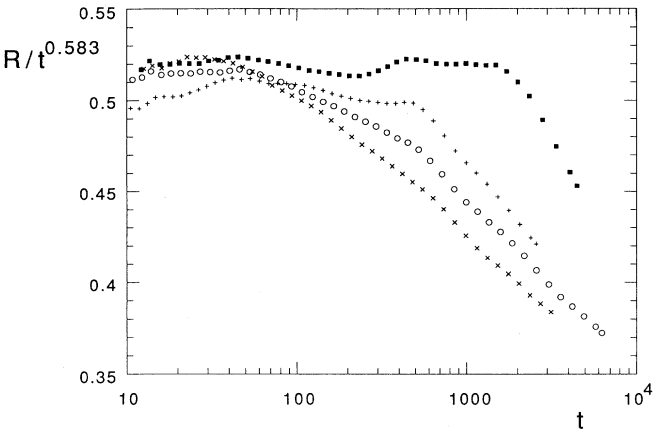

FIG. 10. Plot of $\langle R \rangle / t^{0.583}$ vs t from the smoothed data for central flow, showing the crossover from initial fractal behavior (constant) to eventual compact behavior ($t^{-0.083}$ dependence) on a characteristic time scale τ increasing with viscosity ratio [$M=25$ (×), 50 (○), 100 (+), and 10 000 (■)].

plotting $R/t^{1/D_f}$ versus $(t+\Delta)/M^{D_f\phi_l}$, where the shift $\Delta=1600/M^{D_f\phi_l}$ seems to provide the best collapse of the data. Given the scatter in this data, the scaling is perfectly reasonable, supporting our conjecture that the two-dimensional fractal-to-compact crossover occurs on a length scale which varies asymptotically as $l \approx M^{\phi_l}$, where $\phi_l = 0.24 \pm 0.06$.

VI. CONCLUSIONS

The effect of the viscosity ratio in changing the nature of viscous fingering, where a less viscous fluid is used to displace a more viscous fluid, was studied using a simple, physical model of miscible, dispersionless, two-phase flow in square-lattice, two-dimensional porous media. The absence of surface tension in this miscible two-phase flow placed the focus unambiguously on the effect of viscosity ratio; the absence of dispersion at the interface avoided the interfacial smoothing which would suppress small-scale fluctuations. The resulting simulations have a number of advantages: (i) fluid is conserved to within a fraction of a percent, (ii) decreasing the discrete time step in the numerical integration of the motion of the fluids is statistically insignificant (i.e., does not affect average properties), (iii) the flows for a very large viscosity ratio demonstrated the correct fractal behavior, (iv) the use of a small aspect ratio (short, wide systems) avoids the crossover to pseudostable flow observed in large-aspect-ratio systems, and (v) the overlap of results from porous-media realizations with different lengths shows that finite-size effects were statistically insignificant in these simulations.

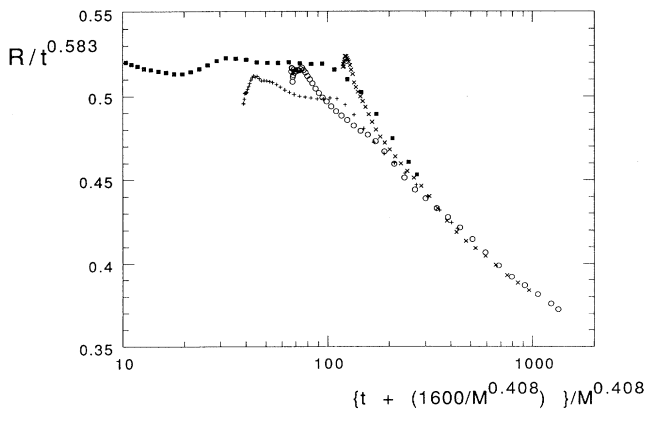

FIG. 11. The scaling plot of $\langle R \rangle / t^{0.583}$ vs $\{t+1600/M^{0.408}\}/M^{0.408}$ for central flow shows that assuming the same length scaling as for linear flow adequately scales the central flow data [$M=25$ (×), 50 (○), 100 (+), and 10 000 (■)].

Real-space renormalization-group (rsrg) approximations estimated that the crossover length should scale linearly with M, i.e., $\phi_l = 1$ [22]; this result also follows from the reasonable assumption that, for all viscosity ratios, there is one flow velocity at the fingertips, while for finite viscosity ratios there is also a second flow velocity, elsewhere on the interface [23]. However, the quantitative analysis of our flow simulations cannot be described with a crossover length varying linearly with M, and the qualitative change in behavior from the early-stage fractal growth to the midstage growth at small distance scales (Fig. 6) is not consistent with a smaller uniform second flow along the interface. Therefore, quantitatively and qualitatively our simulations are in striking disagreement with earlier approximate treatments of this crossover.

For all viscosity ratios, the initial flows had an unstable, fractal character which crossed over (relaxed) to stable, compact flow on a time (or length) scale which increased with the viscosity ratio. Empirical scaling of the data enabled an asymptotic characterization of the viscosity-ratio dependence of (i) the characteristic length scale for both linear and radial geometries $l \approx M^{\phi_l}$ where $\phi_l = 0.24 \pm 0.06$; (ii) the characteristic time scale, in linear flow $\tau \approx M^{\phi_t}$, where $\phi_t = 0.17 \pm 0.03$ and $\phi_t = \phi_l(D_f - 1)$; (iii) the linear flow front velocity $v \approx M^{\epsilon\phi_t}$, where $\phi_t = 0.17 \pm 0.03$ and $1+\epsilon = 1/(D_f - 1)$, so that $\epsilon\phi_t = 0.07 + 0.02$; and (iv) the characteristic time scale for radial flow, $\tau \approx M^{\phi t}$, where $\phi_t \approx 0.41$ and $\phi_t = \phi_l D_f$.

In two dimensions, the crossover characterizing the relaxation from initial, unstable fractal flow to final, stable flow shows a fractal overshoot and an intermediate, overdense regime during which the front advances more slowly than linearly. That is, during the relaxation to stable flow, there is a period of growth at the interior of the pattern (i.e., small distance scales); throughout this overdense growth, some of the voids formed during the fractal stage of growth are being filled in. The character of this postovershoot, overdense growth was observed qualitatively from typical "growth-zone" patterns as well as qualitatively from the average position of the growth sites, $\langle x \rangle_G$.

We are investigating a number of obvious extensions of this work. What is the effect of mixing of the fluids on

the crossover? How does the crossover behave in three dimensions? Although the real "pore-throat" distributions are quite broad, all cross-sectional areas are not equiprobable as we have assumed [24]. What is the effect of more realistic pore-throat distributions?

ACKNOWLEDGMENTS

M.F. gratefully acknowledges support from the National Research Council during the initial stages of this work. We also acknowledge the support of the Fossil Energy program, U.S. Department of Energy, partly through the appointment of M.F. to the Part-Time Faculty Research Participation Program administered by Oak Ridge Associated Universities.

APPENDIX: DETERMINING THE EFFECTIVE TIME: THE EFFECT OF LATTICE DISCRETENESS UPON THE AVERAGE INTERFACE POSITION

For a large (macroscopic) porous medium, one expects that when even a few percent of available volume has been occupied by the injected fluid, the discreteness of the medium will not affect observations. In a continuum model we can define the first moment of the mass of injected fluid as

$$\langle x \rangle = \int_{x=0}^{L} x \frac{\rho(x)}{m_{\text{tot}}} dx \ , \tag{A1a}$$

where $\rho(x)$ is the linear density profile from $x=0 \rightarrow L$ and where

$$t = m_{\text{tot}} = \int_{x=0}^{L} \rho(x) dx \ . \tag{A1b}$$

However, in our discrete $N_x \times N_y$ square-lattice models of length L_x and width L_y, one does not have a continuous density profile, but rather one has an occupation for each row of lattice sites, i.e., $\rho(i)$ for the ith row, $i=1 \rightarrow N_x$. Therefore, the first moment will be given by the sum

$$\langle x \rangle = \sum_{i=1}^{N_x} ia \frac{\rho(i)}{m_{\text{tot}}} \ , \tag{A2a}$$

where the rows of the lattice are a distance $a = L_x / N_x$ apart and where

$$m_{\text{tot}} = \sum_{i=1}^{N_x} \rho(i) \ . \tag{A2b}$$

At this point, we will choose our length scale so that $a \equiv 1$, which makes both sums and integrals dimensionless and which enables us to treat the integrand and summand interchangeably, i.e., $\rho(i) = \rho(x=i)$. For a very large system ($L \gg 1$), the discreteness of our model is unobservable on a scale of the system size, and the sums in Eqs. (A2) approach the integrals in Eqs. (A1) in the usual way.

However, for small values of $\langle x \rangle$, the discreteness of our lattice model does affect the relationship between $\langle x \rangle$ and $t \equiv m_{\text{tot}}$. Fortunately, quantifying this effect for compact (nonfractal) flow enables us to define an effective time which minimizes these small $\langle x \rangle$ deviations. To understand the genesis of this effective time, we first consider the difference between the sums [Eqs. (A2)] and the integrals [Eqs. (A1)]. For a typical function, the integral

$$A_c = \int_{x=0}^{10} f(x) dx \tag{A3}$$

is equal to the area, A_c, under the continuous curve $f(x)$, while the sum

$$A_D = \sum_{i=1}^{10} f(i) = f(1) + f(2) + f(3) + \cdots + f(9) + f(10) \tag{A4}$$

is equal to the area, A_D, under the stepwise "histogram." Clearly, the integral would be better approximated by a trapezoidal estimate than by the sum in Eq. (A4), that is,

$$\begin{aligned} A_c \approx & \tfrac{1}{2}[f(0)+f(1)] + \tfrac{1}{2}[f(1)+f(2)] + \tfrac{1}{2}[f(2)+f(3)] \\ & + \tfrac{1}{2}[f(3)+f(4)] + \cdots + \tfrac{1}{2}[f(8)+f(9)] \\ & + \tfrac{1}{2}[f(9)+f(10)] \ . \end{aligned} \tag{A5}$$

Graphically, the difference between the estimates in Eqs. (A5) and (A4) (between the value of the sum and the trapezoidal estimate) is equal to the area of the triangular portions above the $f(x)$ minus the area of the triangular portions below the $f(x)$. Algebraically, this is simply Eq. (A4) minus Eq. (A5):

$$A_D - A_c \approx \tfrac{1}{2}[f(10) - f(0)] \ . \tag{A6}$$

The form of effective mass which minimizes discreteness effects is most easily derived for pistonlike displacement (flat interface where $\langle x \rangle = \frac{1}{2}t$). Consider the pistonlike motion of a flat interface through $i=l$; for our $N_x \times N_y$ rectangular lattice, the occupation of a row of pores bodies is N_y, for all rows through the flat interface between $i=l$ and $l+1$. For this case, the mass is the same in both the continuum [$m_{\text{tot},c} = A_c$, Eq. (A1b)] and discrete [$m_{\text{tot},D} = A_D$, Eq. (A2b)] cases, being the area of a rectangle of height N_y and base l,

$$m_{\text{tot},c} = m_{\text{tot},D} = lN_y \ , \tag{A7}$$

since the difference in Eq. (A6) is zero [here, $f(l) = f(0)$]. However, the results for the moment $\langle x \rangle$ differ. From the integral which evaluates the area of a triangle of height lN_y and base l, we have

$$\langle x \rangle_c = \frac{1}{m_{\text{tot}}} (lN_y) \left[\frac{l}{2} \right] = \left[\frac{l}{2} \right] . \tag{A8}$$

Equation (A6) shows us that the sum will give the result

$$\langle x \rangle_D = \frac{1}{m_{\text{tot}}} \left\{ (lN_y) \left[\frac{l}{2} \right] + \tfrac{1}{2}[(lN_y) - 0] \right\} = \frac{l+1}{2} \ , \tag{A9}$$

where the first term in the curly braces results from the integral in Eq. (A8) and the second term results from the excess of Eq. (A6). Therefore, the linear behavior of Eq. (A8) resulting from a continuum model

$$\langle x \rangle_c = \left[\frac{l}{2} \right] = \frac{1}{2} \frac{m_{\text{tot}}}{N_y} \tag{A10}$$

is mimicked for the discrete model

$$\langle x \rangle_D = \left[\frac{l+1}{2} \right] = \frac{1}{2} \left\{ \frac{m_{\text{tot}}}{N_y} + 1 \right\} \tag{A11}$$

if one uses

$$m_{\text{eff}} \equiv t_{\text{eff}} N_y \equiv m_{\text{tot},D} + N_y$$

as an effective-mass variable in the discrete model. This defines effective time used in the analysis of the moments.

Surprisingly, it is possible to verify that this same effective saturation applies for general compact (nonfractal) flow. In this case, where one can write $\rho(x,t)=\rho(x/t)$ because $\langle x \rangle = vt$, evaluating the integrals [Eqs. (A1)] for total mass and first moment both yield results proportional to t:

$$m_{\text{tot},c} = aN_y t \ , \tag{A12}$$

$$\langle x \rangle_c = bt \ , \tag{A13}$$

so that the first moment is proportional to total mass

$$\langle x \rangle_c = \frac{b}{a} \frac{m_{\text{tot},c}}{N_y} \ . \tag{A14}$$

If one has a smooth occupation-density profile $\rho(x/t)$ varying from $\rho(0)=N_y$ to $\rho(x/t)=0$ for $x/t \geq v_{\max}$, Eq. (A6) shows that the discrete evaluation of the total mass is given by

$$m_{\text{tot},D} \approx m_{\text{tot},c} + \tfrac{1}{2}(0-N_y) = aN_y t - \tfrac{1}{2}N_y \ , \tag{A15}$$

while the discrete evaluation of the un-normalized moment gives the same result as the integral:

$$m_{\text{tot},D} \langle x \rangle_D \approx m_{\text{tot},c} \langle x \rangle_c + \tfrac{1}{2}(0-0) = (aN_y t)(bt) \ , \tag{A16}$$

since the integrand $x\rho(x)$ is zero at both limits of integration. Using Eq. (A15) to replace $(aN_y t)$ by $m_{\text{tot},D} + \frac{1}{2}N_y$ in Eq. (A16), one finds

$$\langle x \rangle_D \approx \frac{b}{aN_y} \frac{(m_{\text{tot},D} + \frac{1}{2}N_y)^2}{m_{\text{tot},D}} \approx \frac{b}{aN_y} \{ m_{\text{tot},D} + N_y \} \ , \tag{A17}$$

where we neglect the quadratic term $\{\frac{1}{2}N_y\}^2/m_{\text{tot},D}$ because it is of order t^{-1}, whereas the two terms retained are of order t^{+1} and t^0. In Eq. (A17), note that this is simply our definition of effective mass:

$$t_{\text{eff}} \equiv \left\{ \frac{m_{\text{tot},D}}{N_y} + 1 \right\} \ , \tag{A18}$$

so that

$$\langle x \rangle_c = \frac{b}{a} t_{\text{eff}} \ . \tag{A19}$$

This provides a first-order correction to the difference between continuous and discrete determinations. Therefore, use of the effective saturation (or effective time) enables us to reduce the small time and distance effects of discreteness upon the relation between the first moment and the mass.

If the mass pattern is fractal, one can proceed in a similar fashion, realizing that the equation for the first moment from the continuous evaluation becomes in Eq. (A13),

$$\langle x \rangle_c = bt^{1+\epsilon} \ ,$$

while the equation for the total mass in Eq. (A12) as well as the relations between the discrete and continuous evaluations, Eqs. (A15) and (A16) remain unchanged. Replacing the (bt) by $(bt^{1+\epsilon})$ in Eq. (A16) and using Eq. (A15) to replace $(aN_y t)$ by $m_{\text{tot},D} + \frac{1}{2}N_y$, one finds

$$\langle x \rangle_D \approx \frac{b}{aN_y} \frac{(m_{\text{tot},D} + \frac{1}{2}N_y)^{2+\epsilon}}{m_{\text{tot},D}} \ . \tag{A20}$$

Assuming that $t_{\text{eff}} = (m_{\text{tot},D}/N_y) + c$, one can determine the constant c by requiring that the correction to first order in $1/t_{\text{eff}}$ vanish, that is, using this definition of t_{eff} in Eq. (A20), one finds

$$\begin{aligned} \langle x \rangle_D &\approx \frac{bN_y^{\epsilon}}{a} \frac{(t_{\text{eff}} - c + \frac{1}{2})^{2+\epsilon}}{t_{\text{eff}} - c} \\ &= \frac{bN_y^{\epsilon}}{a} t_{\text{eff}}^{1+\epsilon} \frac{\{1 - t_{\text{eff}}^{-1}(c - \frac{1}{2})\}^{2+\epsilon}}{1 - t_{\text{eff}}^{-1} c} \ . \end{aligned} \tag{A21}$$

Expanding in powers of t_{eff}^{-1}, we find

$$\begin{aligned} \langle x \rangle_D \approx \frac{bN_y^{\epsilon}}{a} t_{\text{eff}}^{1+\epsilon} \{ 1 + t_{\text{eff}}^{-1} [-(2+\epsilon)(c - \tfrac{1}{2}) + c] \\ + O(t_{\text{eff}}^{-2}) \} \ . \end{aligned} \tag{A22}$$

Requiring that the coefficient of t_{eff}^{-1} be zero determines the value of c, in t_{eff}

$$t_{\text{eff}} = \frac{S_{\text{tot},D}}{N_y} + \frac{1}{2} \frac{2+\epsilon}{1+\epsilon} \ . \tag{A23}$$

Therefore, use of this effective time in a discrete model accounts for the difference between sums and integrals through first order in t_{eff}^{-1}.

For the model discussed in this paper, there are N_y throats parallel to the x axis at $x = 2m+1$, containing a total volume $\frac{1}{2}N_y$, as well as pore bodies and throats parallel to the y axis at $x = 2m$, containing a total volume $\frac{3}{3}N_y$. When one reproduces the pistonlike discussion for this model, one finds for compact flow,

$$t_{\text{eff}} = m_{\text{tot},D}/N_y + 1.5 \ ,$$

whereas for fractal flow, where $\epsilon = 0.4$,

$$t_{\text{eff}} = m_{\text{tot},D}/N_y + 1.3 \ .$$

The latter definition with the additive factor of 1.3 was used in the analysis of Secs. II and III and does reduce the early time curvature due to the difference between discrete and continuous models.

*Permanent address: Physics Dept., W. Va. Univ., Morgantown, WV 26506.
†E. G. & G.
‡U.S. Department of Energy.
§Also at Institute for Applied Surfactant Research, and School of Chemical Engineering and Materials Science, University of Oklahoma, Norman, OK.

[1] P. Meakin, Phys. Rev. A **27**, 604 (1983).
[2] J.-D. Chen and D. Wilkinson, Phys. Rev. Lett. **55**, 1892 (1985).
[3] G. Daccord, J. Nittmann, and H. E. Stanley, Phys. Rev. Lett. **56**, 336 (1986).
[4] J. Lenormand, E. Touboul, and C. Zarcone, J. Fluid Mech. **189**, 165 (1988).
[5] M. Cieplak and M. O. Robbins, Phys. Rev. Lett. **60**, 2042 (1988).
[6] T. Vicsek, *Fractal Growth Phenomena* (World Scientific, Singapore, 1989).
[7] M. J. King and H. Scher, Phys. Rev. A **41**, 874 (1990).
[8] H. Siddiqui and M. Sahimi, Chem. Eng. Sci. **45**, 163 (1990).
[9] P. W. Barker and R. C. Ball, Phys. Rev. A **42**, 6289 (1990).
[10] J. F. Fernandez, R. Rangel, and J. Rivero, Phys. Rev. Lett. **67**, 2958 (1991).
[11] R. J. Blackwell, J. R. Rayne, and W. M. Terry, Trans. AIME **216**, 1 (1959).
[12] P. Meakin, Phys. Rev. A **27**, 1495 (1983).
[13] R. E. Collins, *Flow of Fluids through Porous Materials* (Reinhold, New York, 1961).
[14] H. E. Stanley, *Introduction to Phase Transitions and Critical Phenomena* (Oxford University Press, New York, 1971).
[15] M. Ferer, W. N. Sams, R. A. Geisbrecht, and D. H. Smith, Physica A **177**, 273 (1991); and Society of Petroleum Engineers No. 25270, Proceedings of the 12th Symposium on Reservoir Simulation, New Orleans, LA (SPE, Richardson, TX, 1993).
[16] M. Ferer, R. A. Geisbrecht, W. N. Sams, and D. H. Smith, Phys. Rev. A **45**, R6973 (1992).
[17] For constant injection, the mass is simply proportional to the time; given an appropriate pressure rescaling (which could be absorbed into Δt) at each cycle, we could have recast our simulation as one of constant injection. Therefore, the mass provides a time scale for these simulations.
[18] B. B. Mandelbrot, *The Fractal Geometry of Nature* (Freeman, New York, 1982).
[19] J. Feder, *Fractals* (Plenum, New York, 1988).
[20] I. Fatt, Trans. AIME **207**, 144 (1956).
[21] P. R. King, J. Phys. A **20**, L529 (1987).
[22] J. Lee, A. Coniglio, and H. E. Stanley, Phys. Rev. A **41**, 4589 (1990).
[23] R. Lenormand, Proc. R. Soc. London, Ser. A **423**, 159 (1989).
[24] C. E. Krohn, J. Geophys. Res. 93, 3286 (1988).